PHYSICAL REVIEW E **106**, 035102 (2022)

Instabilities of the natural convection around a cone in thermally stratified medium

Yue Xiao, Yi Li, Moli Zhao, and Shaowei Wang*
Department of Engineering Mechanics, School of Civil Engineering, Shandong University, Jinan 250061, People's Republic of China

(Received 6 April 2022; accepted 6 September 2022; published 14 September 2022)

In this paper, we provide a mathematical description of the onset of instability for buoyancy-driven flow around a cone. The self-similar solutions of the basic flow are derived, where the ambient fluid and the cone have independent temperature gradients. The linear instability properties are investigated by utilizing the Chebyshev collocation method. It is demonstrated that the neutral curves have a two-lobed structure and that changing the Grashof number has only quantitative influence on stability. The critical streamwise location increases when the half-apex angle is increased, and the unstable range of the wave number diminishes. According to the examination of eigenfunction profiles and the progression of the two spatial branches in the (α_i, α_r) planes, the primary instabilities on the surface of cone are identified as type-I mode and type-II mode. The energy analysis is investigated for a typical situation to gain a physical insight, where it is demonstrated that besides the viscous dissipation, the streamline curvature and buoyancy-driven effects are dominant for the type-I mode while inviscid effect plays an essential role in type II. These encouraging results are expected to be conducive to understanding buoyancy-driven systems.

DOI: 10.1103/PhysRevE.106.035102

I. INTRODUCTION

Flows induced by buoyancy forces in the stratified ambient fluid are very common in several industrial processes and nature. When an inclined plate is heated or cooled in a stably stratified fluid, a buoyancy-driven boundary layer flow will be generated. Such layers representing a balance between buoyancy and viscous force have been called buoyancy layers, and the inclined buoyancy layer is of particular interest to atmospheric scientists. For example, katabatic winds are formed when the mountain surface becomes colder than the surrounding air, forcing the wind to rush down the slope. This typical case was first investigated by Prandtl [1]. In his study, by assuming a homogeneous boundary layer, a plane parallel flow solution with a reversal velocity profile was derived. The meteorological literature has focused on daily and seasonal variations and the effects of actual topographies on the mountain-valley winds—for a review, we refer to the book by Stull [2]. Gill [3] simulated the vertical buoyancy layers in a heated rectangular cavity, the wall of which has the same linear temperature gradients as the ambient fluid. An exact solution was provided and the corresponding flow is parallel and simply one-dimensional both for velocity and temperature fields. The stability of such flows with respect to small disturbances has been of concern for many researchers. Based on Gill's solution, Gill and Davey [4] considered the stability of a buoyancy layer developed over a heated vertical plate and determined the neutral stability conditions for a wide range of Prandtl numbers. Then, the neutral curve for various angles of the inclined case was analyzed based on linear and weakly nonlinear stability analysis [5,6], respectively. For the linear case, two types of instabilities have been studied: the transverse traveling Tolmien-Schlichting waves (T-S waves) and the longitudinal rolls. Both theoretical studies and experiments for a boundary layer were introduced by Jaluria and Gebhart [7]. In the boundary layer, the temperature difference between the extensive medium and the wall varied downstream with a power law $x^{0.2}$, and the exponent guarantees that the wall will dissipate uniform heat flux. The results suggest that a stable ambient stratification delays the early stages of transition. Their velocity and temperature fields were verified by Jaluria and Himasekhar [8] via a finite difference method. In addition, a similarity solution describing the boundary layer around an isothermally heated plate was obtained by Kulkarni *et al.* [9]. Based on this solution, linear instability was analyzed later by Krizhevsky *et al.* [10]. The theoretical and numerical studies of Prandtl's buoyancy layer have made substantial progress [11–15], but mostly on transverse T-S waves. Especially, according to three-dimensional stability analysis [16], the oblique roll mode is found to be more unstable than the transverse T-S wave mode at some inclination angles and Prandtl numbers due to the ambient thermal stratification.

In some special circumstances in geography (e.g., pinnacle mountain or glaciers) and engineering applications (e.g., nuclear reactors, solar power collectors, power transformers, and steam generators), an inclined or vertical plate will no longer be appropriate and the geometric configuration with a conical surface must be considered. The problem of nature convection flow along a vertical cone has been treated in many papers. For example, Merk and Prins [17–19] developed the general relations for similar solutions with axisymmetric forms for an isothermal vertical cone. For cones with prescribed wall temperatures being a power-law function of the distance from the apex along the generatrix, a number of similarity solutions were obtained by Hering and Grosh [20],

---

*shaoweiwang@sdu.edu.cn

whereas Hering [21] extended these solutions to investigate low-Prandtl-number fluids. Na and Chiou [22] presented the laminar natural convection over a frustum of a cone without transverse curvature effect. The effect of transverse curvature on boundary layer flow of a thermomicropolar fluid past a slender vertical cone was investigated by Gorla *et al.* [23]. It was observed that the heat transfer rate increases with the increasing transverse curvature. Alamgir [24] investigated the free convection on a slender vertical cone with power-law wall temperature variations, and an integral method was used to predict the overall heat transfer. The effect of uniform suction or injection on free convection boundary layer over a cone was investigated by Watanabe [25] theoretically. By assuming that the thermophysical quantities vary with temperature, the laminar steady flow over an isothermal vertical cone was obtained [26,27]. The transient free convection flow past a vertical cone with temperature varying as power function of distance from the apex was studied numerically by Bapuji *et al.* [28]. In all the above-mentioned results of nature convection on a cone, the authors mainly focused on the basic flow solution and the heat transfer performance, but the research of stability for natural-convection around a cone is still very scarce.

It is known that laminar-turbulent transition has a significant effect on heat transfer efficiency, surface friction, and flow control. Moreover, linear stability analysis has been proven a powerful tool to describe the first stage to turbulence. Different from previous studies, in this paper, we propose a vertical cone model, where the cooled cone surface and the ambient fluid have independent vertical temperature gradients. After introducing a modified Grashof number, we obtain a similarity solution and discuss the critical instability. The dominant linear instability mechanisms which cause the laminar-turbulent transition process are analyzed as well. The remainder of this investigation is outlined as follows. Section II describes the mathematical formulation of the fluid problem and the governing equations. The basic flow with similarity form and the local linear stability analysis are described in Secs. III and IV, respectively. Section V discusses the effects of main physical parameters on local instability transition, while an energy analysis of the disturbance field is also carried out in this section. Finally, conclusions are presented in Sec. VI.

II. MATHEMATICAL FORMULATION

The three-dimensional boundary layer induced by buoyancy in stratified fluid is studied, and the flow around an axisymmetric cone with the half-apex angle ψ. A sketch of the geometry and the reference frame is shown in Fig. 1. An orthogonal curvilinear coordinate system with the origin located at the apex of the cone was utilized to write the governing equations, where η^*, θ, and ξ^* are the coordinates along the generatrix of the cone, azimuthal, and wall-normal direction, respectively. The local cross-sectional radius $r^* = \eta^* \sin\psi + \xi^* \cos\psi$.

A stably stratified fluid with density ρ_r, kinematic viscosity ν, coefficient of thermal expansion γ, and thermal diffusivity κ fills the space far away from a cone, which is heated or cooled with respect to the surroundings. The temperature in ambient fluid $T_\infty^*(s^*)$ varies linearly in the vertical direction, $T_\infty^*(s^*) = T_\infty^*(0) + N_\infty^* s^*$, where s^* has the same direction with gravity $\boldsymbol{g}$ and N_∞^* is the temperature gradient in the medium. Different from previous work [16], the wall temperature is decreased by a fixed amount ΔT^* below that of the fluid outside the boundary layer, the temperature on cone surface $T_w^*(s^*)$ also varies linearly but has different temperature gradient $N_w^* < N_\infty^*$, $T_w^*(s^*) = T_\infty^*(0) + N_w^* s^*$. The subscript ∞ and the hyperscript $*$ denote the ambient condition and dimensional quantities, respectively.

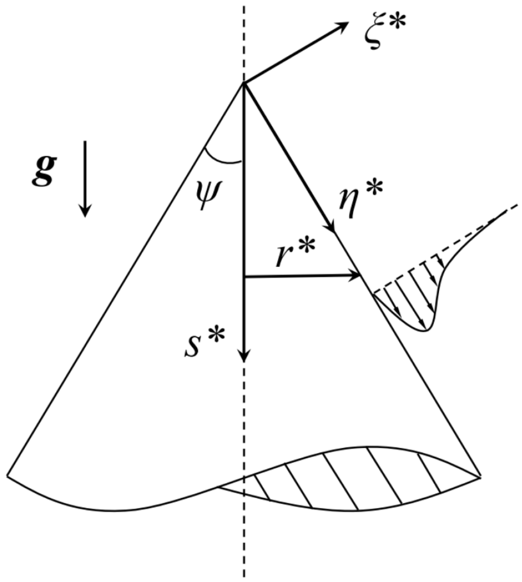

FIG. 1. Schematic geometry of a buoyancy-driven boundary layer.

On the Boussinesq approximation, the governing equations are given by

$$\begin{aligned} &\nabla \cdot \boldsymbol{v}^* = 0, \\ &\frac{\partial \boldsymbol{v}^*}{\partial t^*} + \boldsymbol{v}^* \cdot \nabla \boldsymbol{v}^* = -\nabla\left(\frac{P^*}{\rho_r}\right) - \boldsymbol{g}\gamma(T^* - T_\infty^*) + \nu \nabla^2 \boldsymbol{v}^*, \\ &\frac{\partial T^*}{\partial t^*} + \boldsymbol{v}^* \cdot \nabla T^* = \kappa \nabla^2 T^*. \end{aligned} \tag{1}$$

The dimensionless length, time, and temperature in the present study are defined as

$$(\eta, \xi) = \frac{(\eta^*, \xi^*)}{d}, \qquad t = \frac{t^* \nu}{d^2},$$
$$T = \frac{T^* - T_\infty^*}{(N_w^* - N_\infty^*) s^*}, \qquad d = \left(\frac{4\nu\kappa}{g\gamma \cos^2\psi N_w^*}\right)^{1/4}. \tag{2}$$

The nondimensional parameter of the problem are the Grashof number Gr and the Prandtl number Pr,

$$\mathrm{Gr} = \frac{g\gamma \cos^2\psi (N_\infty^* - N_w^*) d^4}{\nu^2}, \qquad \mathrm{Pr} = \frac{\nu}{\kappa}. \tag{3}$$

Considering the small boundary layer thickness, the radius r^* along the ξ^* direction is assumed constant within the boundary layer, i.e., $r^* \approx \eta^* \sin\psi$. Besides, terms of order $O(\eta^{*-2})$ in Eq. (1) have been discarded in the following analysis without significant deviations when considering the position far away from the apex of the cone.

III. BASIC FLOW ANALYSIS

In this section, we will derive the basic flow within the boundary layer induced by buoyancy. The motion is assumed to be steady and axisymmetric in the following analysis. Under the boundary layer approximation, the continuity equation becomes

$$\frac{\partial v_\eta}{\partial \eta} + \frac{\partial v_\xi}{\partial \xi} + \frac{v_\eta}{\eta} = 0, \tag{4}$$

with the condition of $v_\eta \gg v_\xi$. Since $\xi \sim O(1)$ and $\eta \sim O(\eta_0)$, we note from the continuity equation that there is a possible order for velocity $v_\xi \sim O(1)$ and $v_\eta \sim O(\eta_0)$, where $\eta_0 \gg 1$ represents a nondimensional characteristic scale of the streamwise flow. By comparing the order of each term in the momentum and energy equation carefully, the smaller terms have been omitted and the simplified equations are

$$v_\eta \frac{\partial v_\eta}{\partial \eta} + v_\xi \frac{\partial v_\eta}{\partial \xi} = \eta \mathrm{Gr} T + \frac{\partial^2 v_\eta}{\partial \xi^2}, \tag{5a}$$

$$0 = -\frac{\partial P}{\partial \xi} - \eta \tan\psi \mathrm{Gr} T + \frac{\partial^2 v_\xi}{\partial \xi^2}, \tag{5b}$$

$$\mathrm{Pr}\left[v_\xi \frac{\partial T}{\partial \xi} + \frac{1}{\eta} v_\eta (T-1)\right] - \frac{4}{\eta \mathrm{Gr}} v_\eta = \frac{\partial^2 T}{\partial \xi^2}. \tag{5c}$$

Now, we intend to seek a self-similar solution to reduce the partial differential equations to the ordinary ones. In the present problems Eqs. (4) and (5), one can postulate that

$$v_\eta = f(\eta)F(\xi), \quad v_\xi = g(\eta)G(\xi), \quad T = T(\xi). \tag{6}$$

It is not difficult to show that the self-similar solution is possible if we set $f(\eta) = \eta$ and $g(\eta) = 1$. Substituting Eq. (6) into Eqs. (4) and (5), we obtain

$$2F + G' = 0, \tag{7a}$$

$$F^2 + GF' = \mathrm{Gr} T + F'', \tag{7b}$$

$$\mathrm{Pr}[GT' + F(T-1)] - \frac{4}{\mathrm{Gr}} F = T'', \tag{7c}$$

where the prime indicates $d/d\xi$, and the boundary conditions are

$$F(0) = G(0) = F(\infty) = T(\infty) = 0, \quad T(0) = 1. \tag{8}$$

Thus, the velocity profiles are fully specified by the Grashof number Gr and the Prandtl number Pr. It is now seen that the above equations and the boundary conditions share a similar form in the von Kármán solution of the rotating disk (cone) problem [29–31]. It is worth noting that there is no explicit parameter ψ in Eqs. (7), which means the self-similar solution is independent of ψ and the effect of ψ will not be considered in this section.

Numerical solution of the system of Eqs. (7) is obtained using the following procedure. The two velocity components [$F(\xi)$ and $G(\xi)$] and temperature ($T(\xi)$) are defined on the semi-infinite physical domain $\xi \in [0, \infty)$, and mapped onto the Chebyshev domain $y \in [-1, +1]$ for computation via the coordinate transformation

$$y = \frac{2}{L_{\max}}\xi - 1,$$

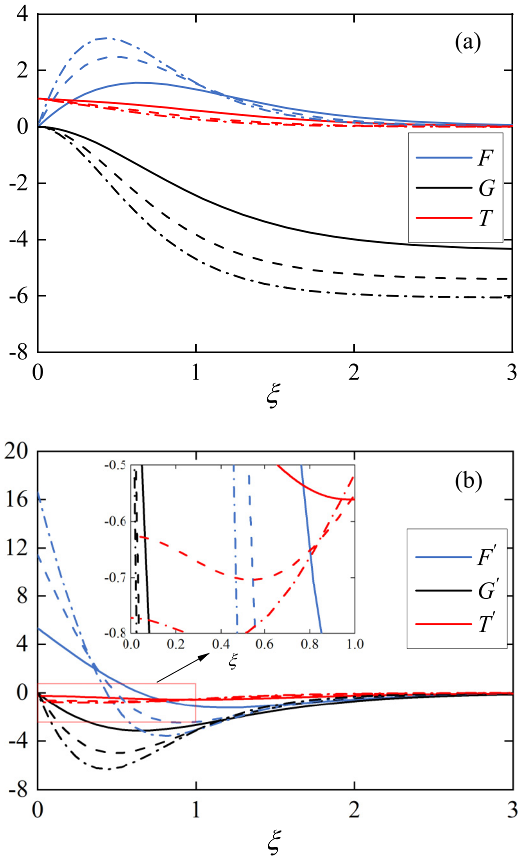

FIG. 2. (a) Velocity profiles F (blue lines), G (black lines), and T (red lines) as functions of the wall-normal direction, for fixed $\mathrm{Pr} = 0.7$ and different value of Gr. The solid lines, dashed lines, and dash-dotted lines indicate the results for $\mathrm{Gr} = 10$, 30, and 50, respectively. (b) Numerical value of the basic flow field F', G', and T' lines represent the same parameters as shown in (a). The inset in panel (b) shows a local enlarged view in the red box.

where $L_{\max}$ is the distance from the ξ axis and a value of $L_{\max} = 15$ is found to be sufficiently large for all unstable modes discussed in this paper. Equations (7) are discretized on Chebyshev points by utilizing Chebyshev differentiation matrices and corresponding boundary conditions. Additionally, it is worth noting that the problem is nonlinear, so an iterative approach is adopted by adding a time-derivative term into the last two equations of Eqs. (7). Then, all spatial terms are treated explicitly via a predictor-corrector method for an appropriate initial guess. In all subsequent numerical calculations, 100 Chebyshev points are used to accurately compute the velocity and temperature. Several tests have been performed for more Chebyshev points and larger computational domain to ensure numerical convergence.

Figure 2(a) shows the two velocities (F and G) and temperature (T) as a function of the wall-normal coordinate for different values of Gr, and Fig. 2(b) gives the numerical values of the basic flow field F', G', and T'. It is shown that G and T decrease monotonously with increasing values of ξ. The negative sign of G suggests the flow outside the boundary layer is pulled toward the cone surface and the wall-normal velocity increases with increasing ξ for a given Gr. This is to be expected physically, as the temperature near the surface is lower than the surroundings, the fluid descends to be replaced by a downward flow through the interaction between gravity and buoyancy. It is also seen that, for a fixed wall-normal position ξ, the increase of Gr results in a larger decay rate for F and T, and higher value of wall-normal velocity at infinity, indicating a thinning of the buoyancy boundary layer.

IV. LOCAL LINEAR STABILITY ANALYSIS

The linear perturbation equations are solved in a parallel framework at several η locations. The nondimensional variables are $v_\eta = v_{\eta 0} + \tilde{v}_\eta$, $v_\theta = v_{\theta 0} + \tilde{v}_\theta$, $v_\xi = v_{\xi 0} + \tilde{v}_\xi$, and $T = T_0 + \tilde{T}$, where $\tilde{v}_\eta, \tilde{v}_\theta, \tilde{v}_\xi$, and $\tilde{T}$ are perturbations and $v_{\eta 0}, v_{\theta 0}, v_{\xi 0}$, and T_0 constitute the undisturbed basic flow solution. Perturbations $\tilde{q}(\eta, \theta, \xi, t)$ for modal analysis are decomposed into the form

$$\tilde{q}(\eta, \theta, \xi, t) = \hat{q}(\xi)\exp\left(i(\alpha\eta + n\theta - \omega t)\right), \tag{9}$$

where $\alpha = \alpha_r + \mathrm{i}\alpha_i$ is the complex wave number in the streamwise direction, while $n \in \mathbb{N}$ and $\omega \in \mathbb{R}$ are the mode numbers in circumferential direction and frequency, respectively. The perturbation equations governing the stability of basic state Eqs. (6) are

$$D\hat{v}_\xi + i\beta\hat{v}_\theta + \left(i\alpha + \frac{1}{\eta}\right)\hat{v}_\eta + \frac{1}{\eta\tan\psi}\hat{v}_\xi = 0, \tag{10a}$$

$$\left(\mathcal{L}_1 + F + \frac{G}{\eta\tan\psi}\right)\hat{v}_\theta + i\beta\hat{p} = 0, \tag{10b}$$

$$(\mathcal{L}_1 + F)\hat{v}_\eta + \eta DF\hat{v}_\xi - \eta\mathrm{Gr}\hat{T} + i\alpha\hat{p} = 0, \tag{10c}$$

$$(\mathcal{L}_1 + DG)\hat{v}_\xi + \eta\tan\psi\mathrm{Gr}\hat{T} + D\hat{p} = 0, \tag{10d}$$

$$\begin{aligned}&\eta\mathrm{Pr}^{-1}\mathcal{L}_2\hat{T} + \left(T - 1 - \frac{4}{\mathrm{PrGr}}\right)\hat{v}_\eta\\ &+\left[\eta DT - \tan\psi(T-1) + \frac{4\tan\psi}{\mathrm{PrGr}}\right]\hat{v}_\xi = 0,\end{aligned} \tag{10e}$$

where $D \equiv d/d\xi$, $\mathcal{L}_1$, and $\mathcal{L}_2$ are linear operators

$$\begin{aligned}\mathcal{L}_1 = {}& \alpha^2 + \beta^2 + i\alpha\left(\eta F - \frac{1}{\eta}\right) - i\omega\\ &+ \left(G - \frac{1}{\eta\tan\psi}\right)D - D^2,\end{aligned} \tag{11a}$$

$$\begin{aligned}\mathcal{L}_2 = {}& \alpha^2 + \beta^2 + i\alpha\left(\eta\mathrm{Pr}F - \frac{1}{\eta}\right) - i\mathrm{Pr}\omega\\ &+ \left(\mathrm{Pr}G - \frac{1}{\eta\tan\psi}\right)D - D^2,\end{aligned} \tag{11b}$$

with $\beta = n/(\eta\sin\psi)$, and the boundary conditions are given by

$$\begin{aligned}&\hat{v}_\eta(0) = \hat{v}_\theta(0) = \hat{v}_\xi(0) = D\hat{p}(0) = \hat{T}_\eta(0) = 0,\\ &\hat{v}_\eta(\infty) = \hat{v}_\theta(\infty) = \hat{v}_\xi(\infty) = D\hat{p}(\infty) = \hat{T}_\eta(\infty) = 0.\end{aligned} \tag{12}$$

Note that the Eqs. (10) have terms as function of η, because the linear stability analysis of the flow applied at a particular streamwise direction position. This procedure is commonly used to analyze the stability of quasiparallel flow, such as the problem of rotating disk [30]. The stability problem Eqs. (10) and (12) constitute an eighth-order differential equation with eight boundary conditions, given by the dispersion relationship

$$\mathcal{F}(\omega, \alpha;\ \mathrm{Gr}, \eta, n, \psi) = 0, \tag{13}$$

which are solved by a spectral collocation method based on Chebyshev polynomials. The eigenfunctions expanded in Chebyshev series are substituted into Eqs. (10) and (12), which are discretized at the Gauss-Lobatto points and solved by the QZ method. The number of Chebyshev polynomials and the computational domain are consistent with Sec. III. For the spatial analysis, we mean to solve the set of equations for α given azimuthal mode number n and frequency ω. However, we are still faced with a nonlinear generalized eigenvalue problem, in which the eigenvalue α appears up to second power in linear operators $\mathcal{L}_1$ and $\mathcal{L}_2$. Here, a transformation of the independent variable ξ of the form [32] $\hat{q}(\xi) = \hat{Q}(\xi)\exp(-\alpha\xi)$ is utilized to reduce the order of the nonlinear eigenvalue problem to a linear one.

V. RESULTS AND DISCUSSION

A. Convective instability

Spatial analysis of the dispersion relationship Eq. (13) is based on the Grashof number Gr, streamwise location η, azimuthal mode number n, and half-apex angle ψ. Since critical value parameters play a significant role in the early stages of laminar-turbulent transitions, the following analysis is concentrated mainly on the neutral curve by setting the complex-valued wave number $\alpha_i = 0$.

Figure 3 displays neutral stability curves for nonstationary disturbances in both the (η, ω) and (η, α_r) planes, with the Grashof number Gr = 10 in Figs. 3(a) and 3(b) and Gr = 50 in Figs. 3(c) and 3(d) for $\psi = 40°$. Despite resulting from different Grashof numbers, all collections of neutral curves display the same qualitative behavior: First, it turns out that the minimum of η for the most unstable modes does not correspond to stationary modes ($\omega = 0$) but to a definite frequency. Unlike the situation in rotating disks [30] and cones [31], where the stationary vortices can rotate with the surface, there is no stationary mode in the current study. And the most unstable modes correspond to $n = 0$, which is also quite different from the previous research on inclined buoyancy layers with fixed temperature plates [16], where the oblique rolls are more unstable than stationary longitudinal rolls. For a given Gr, the critical η and frequency ω increase with increasing values of n. The second interesting development is the two-lobed structure on the curves. Nachtsheim [33] found a very similar two-lobed structure (also known as the nose-shaped piece) for the flux-plate problem with Pr = 0.733, which was shown by him to disappear when buoyancy effects on the instability were ignored. The same feature is mentioned in rotating disks [30], where the neutral stability curves have a two-lobed structure which corresponds to the crossflow instability mode [31] and convectively unstable mode caused by streamwise curvature and Coriolis effect [34]. Besides, the absence of stationary instability modes and the bimodal type of neutral curves are very similar to that obtained in the problem of instability of stationary flow between two vertical plates maintained at different temperatures in the presence of

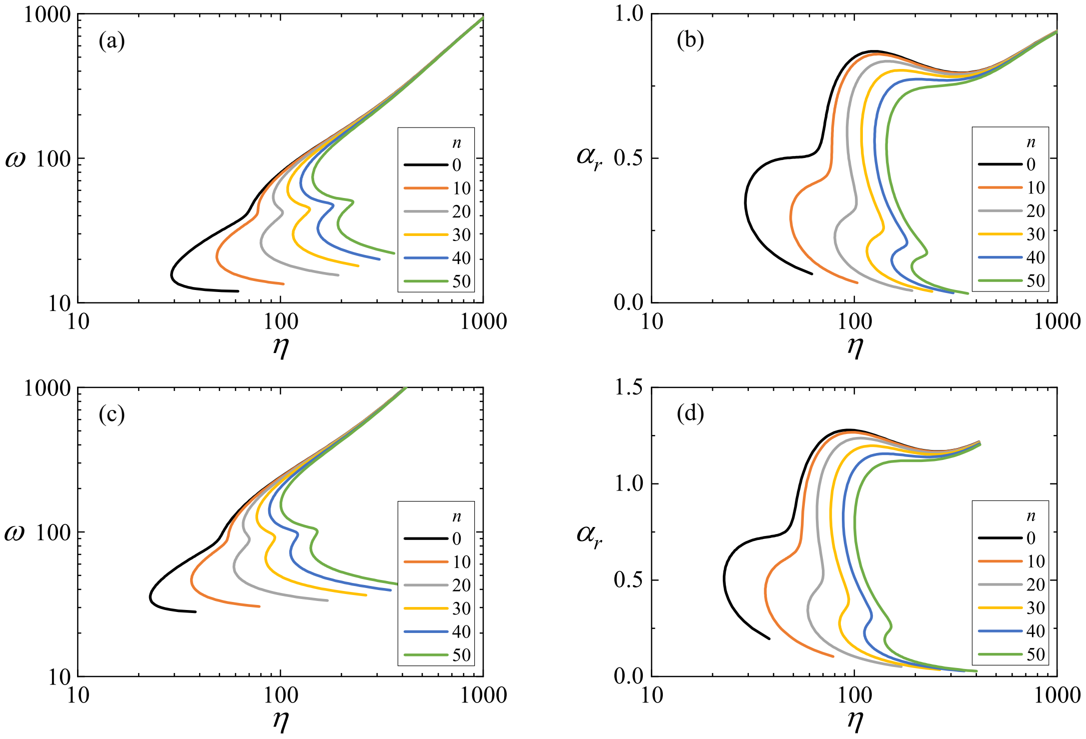

FIG. 3. Neutral stability diagrams for Gr = 10 (first row) and Gr = 50 (second row) with $\psi = 40^\circ$. The neutral curves are shown in (a), (c) (ω, η) planes and (b), (d) (α_r, η) planes.

uniformly distributed heat sources [35,36]. The mechanisms indicated by lobe structures in the present study will be analyzed in detail later. As can be seen from Fig. 3, although Grashof numbers change by 5 times, the basic laws of the two cases are consistent qualitatively. The similarity of all data at different Gr suggests that different Gr only have a quantitative difference in stability characteristics. Hence, a fixed value of Gr = 30 will be used for analysis in the following discussion.

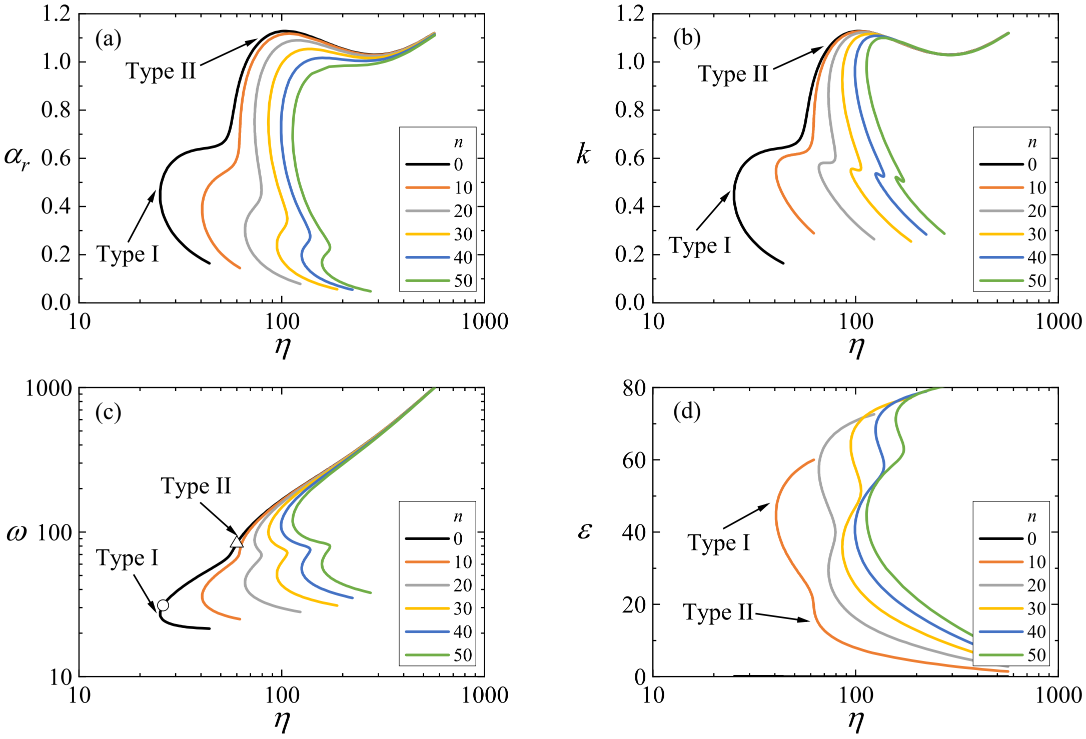

FIG. 4. Neutral stability diagrams for Gr = 30 and $\psi = 40^\circ$. The neutral curves are shown in the (a) (α_r, η) plane, (b) (k, η) plane, (c) (ω, η) plane, and (d) (ε, η) plane (ε is in degrees). Type-I and -II modes are marked with their respective numbers.

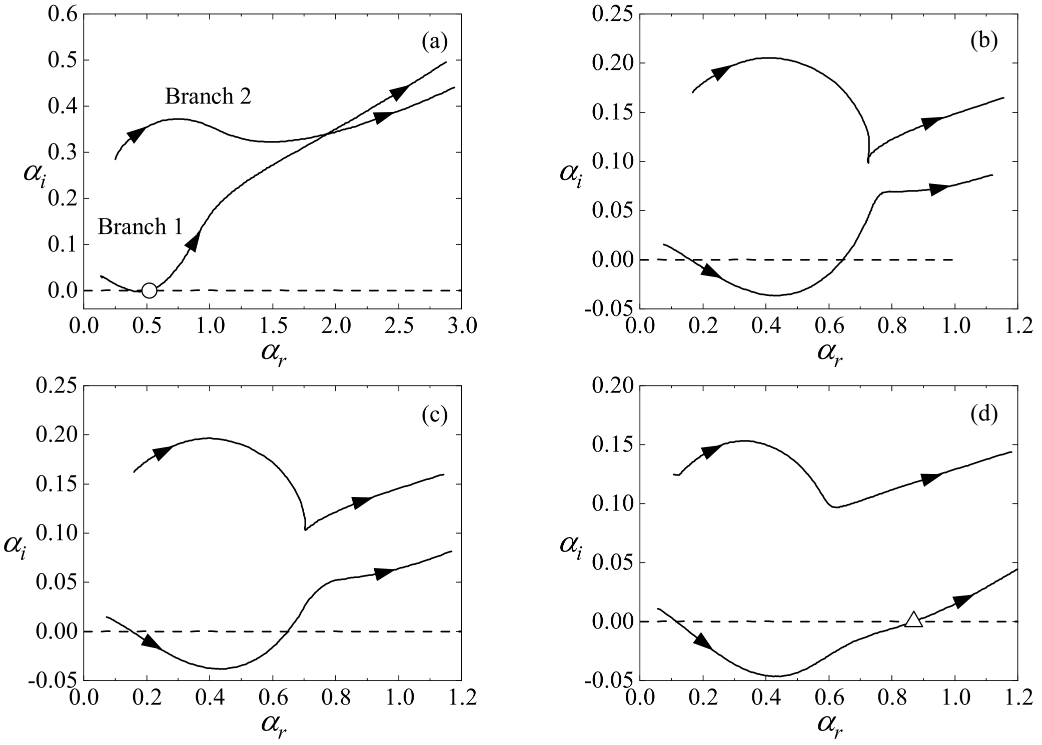

FIG. 5. The progression of the two spatial branches in the (α_i, α_r) planes given by several different values of η for Gr $= 30$, $n = 0$, and $\psi = 40^\circ$: (a) $\eta = 26$, (b) $\eta = 45$, (c) $\eta = 47$, and (d) $\eta = 60$. Two neutral modes are marked with a circle (◯) $(\omega, \alpha_r) = (31.13, 0.52)$ in (a) and triangle (△) $(\omega, \alpha_r) = (83.51, 0.87)$ in (d). These two typical points are also shown in Fig. 4(c). The arrows on the spatial branches indicate the direction of increasing ω.

The neutral curves arising from the analysis of Gr $= 30$ and $\psi = 40^\circ$ are shown in Fig. 4. The unstable region lies inside the curves (right hand side). By comparison with Figs. 3 and 4, it can be seen that with the increase of Gr, the critical location η for convective instability becomes smaller. This is due to the fact that η and Gr appear as a product in the dispersion relation. In addition, the critical η increases with the increase of mode number n in the circumferential direction, suggesting that modes with large n amplify less rapidly. In Fig. 4(a), we observe that the neutral curves have higher and lower wave-number parts, which is similar to the natural convective boundary layers in a uniform medium. As explained by Gill and Davey [4], the higher wave-number part is a result of shear instability and apparently does not change when the buoyancy effect is neglected. The lower part is caused by the coupling between the Orr-Sommerfeld equation and the energy equation which corresponds to a buoyancy-driven instability. The basic flow here is three-dimensional, so the competition between viscous, buoyancy, and effect of streamline curvature will be shown in the energy analysis.

Besides, Fig. 4 also illuminates neutral curves for the angle of the vortex axis with respect to the downstream direction $\varepsilon = \arctan(\beta/\alpha_r)$ and wave number $k = (\alpha_r^2 + \beta^2)^{\frac{1}{2}}$ resolved in the direction of ε. It is shown that the critical value of ε rises significantly with the increase of n when $n < 30$ while k

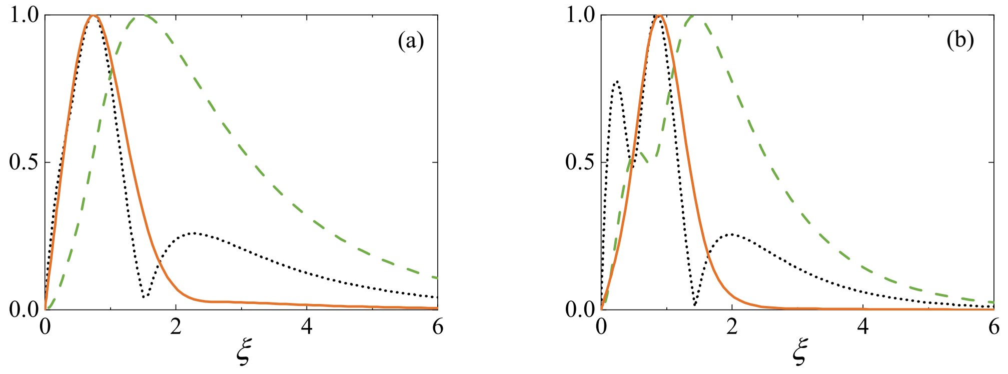

FIG. 6. Normalized amplitude profiles of eigenfunctions for (a) type-I mode and (b) type-II mode as functions of ξ. The dotted lines indicated the results $|\hat{v}_\eta|/|\hat{v}_\eta|_{\max}$. The data $|\hat{v}_\xi|/|\hat{v}_\xi|_{\max}$ and $|\hat{T}|/|\hat{T}|_{\max}$ are given by the dashed and solid lines, respectively.

does not change much. When n is greater than 30, $k \approx 1$ and ε increases as n increases. With n increasing from 0 to 50, the dominant mode of the neutral curve changes from type I to type II, implying that the critical parameters are controlled by different mechanisms.

To investigate the spatial branches at a fixed half angle (e.g., $\psi = 40^\circ$ shown in Fig. 5), we solve the dispersion relation for α whilst marching through values of ω at fixed $\mathrm{Gr} = 30$. Two spatial branches are found to determine the convective instability characteristics of the system. Figure 5 shows these two branches in the complex (α_r, α_i)-planes in the range of $\eta = 26 \sim 60$. An exchange of modes between branch 1 and branch 2 has occurred at $\eta = 45$, as shown in Fig. 5(b). A branch lying below the α_r axis indicates convective instability. The bulge on modified branch 1 move downward when increasing the value of η further and causes the points at which the growth rate $\alpha_i = 0$ to move apart [see Fig. 5(d)]. Thus, the two regions of instability map out two lobes on the neutral curve, and we identify the lower lobe of the neutral curve as type-I instability and the upper lobe as type-II instability.

We first consider the eigenfunctions on the lower and upper lobes of the neutral curve, which may also provide some clues to help identify the mechanisms responsible. Two typical eigenvalues corresponding to type-I -II modes are marked with a circle (◯) for parameters $(\eta, \omega, \alpha_r) = (26, 31.13, 0.52)$ in Fig. 5(a) and triangle (△) $(\eta, \omega, \alpha_r) = (60, 83.51, 0.87)$ in Fig. 5(d), respectively. These two neutral modes are also shown in Fig. 4(c).

Eigenfunctions for type-I -II modes are illustrated in Fig. 6. We make a comparison between the eigenfunctions and the basic flow. First, it is noted that the temperature disturbances are significantly confined to the boundary layer ($\xi \lessapprox 2$) while velocity disturbances spread over a much wider region ($\xi \lessapprox 6$). And the maximum amplitude position of perturbation temperature coincides with that of the streamwise velocity. The two types of modes also have different characteristics. For the type-II mode, close examination reveals that the largest amplitude of the streamwise velocity lies at $\xi_L = 0.87$, which is almost in the same position as the inflection point $\xi_I = 0.90$ in the basic flow $v_{\eta 0}$. The critical phase velocity $c_r = 96$ at the point marked with a triangle in Figs. 4(c) and 5(d) is approximately consistent with the basic streamwise velocity $v_{\eta 0}(\xi_I) = 103$ at the inflection point. For the type-I mode, the maximum amplitude position of the streamwise velocity disturbance is close to that of $v_{\eta 0}$ in basic flow. And the critical phase velocity $c_r = 59.9$ and the maximum streamwise velocity of the basic flow $v_{\eta 0} = 64.5$ are almost identical. These two different characteristics were explained by Gill [4] and Tao [14] as a result of buoyancy-driven instability (type-I mode) and shear instability (type-II mode), respectively. It is also reported that the properties of the absolute instability are dominated by the shear instability [14].

The influence of half-angle ψ on stability is also analyzed with four typical cases: $\psi = 20^\circ, 40^\circ, 60^\circ$, and 80°. Neutral stability curves are shown in Fig. 7 for various half-apex angles ψ. The results show that increasing ψ causes an increase of the critical streamwise location at the onset of convective instability. It is also illustrated that, for a fixed n (e.g., $n = 50$), the most unstable mode may be associated with type II when $\psi = 20^\circ$. However, the dominant mode changes to type I with the increase of ψ [see Fig. 7(d)]. The effect of half-angle ψ on critical wave number is shown in the second column in Fig. 7. For all values of calculated n, increasing the half angle reduces the range of unstable wave number. Additionally, the critical wave angle is always 0 (the line overlaps with the η axis), because the critical streamwise location corresponds to $n = 0$. For $n = 10$, ε decreases monotonically with the increase of ψ. Table I summarizes the critical values of parameters shown in Fig. 7, where we present the critical streamwise location (η), the critical frequency (ω_c), the critical wave number (α_{rc}) in the streamwise direction, and the phase velocity (c), as well as the maximum streamwise velocity of the basic flow $v_{\eta 0}$. By comparing the last two columns, we can observe that $c > v_{\eta 0}$ for $\psi \geqslant 60^\circ$. It is well-known that the critical wave velocity must be smaller than the maximum velocity of the basic flow in the case of inviscid, homogeneous, parallel shear flows. Therefore, the result of $c > v_{\eta 0}$ is due to the influence of buoyancy arising from the basic flow temperature field.

B. Energy analysis

The destabilization of fluid disturbance is usually affected by the various energy transfer mechanisms. To extract possible underlying physical mechanisms behind the stability of buoyancy layer, an integral energy equation for three-dimensional disturbances $\tilde{v}_\eta, \tilde{v}_\theta, \tilde{v}_\xi$, and $\tilde{T}$ to the undisturbed three-dimensional basic flows $v_{\eta 0}, v_{\theta 0}, v_{\xi 0}$, and T_0 is derived. Following the procedure of Cooper *et al.* [37], the energy equation is formulated by multiplying the three linearized momentum equations by the respective perturbation velocities $\tilde{v}_\eta, \tilde{v}_\theta$, and $\tilde{v}_\xi$, and summing together to give the following kinetic energy equation. By integrating across the boundary layer from $\xi = 0$ to $\xi = \infty$, the resulting equation is

$$\int_0^\infty \frac{\partial K}{\partial t} + \underbrace{v_{\eta 0}\frac{\partial K}{\partial \eta}}_{\mathrm{A}} d\xi = \underbrace{\int_0^\infty \left(-\tilde{v}_\eta \tilde{v}_\xi \frac{\partial v_{\eta 0}}{\partial \xi} - \tilde{v}_\xi^2 \frac{\partial v_{\xi 0}}{\partial \xi}\right) d\xi}_{\mathrm{I}} + \underbrace{\int_0^\infty \left(\tilde{v}_\theta \frac{\partial^2 \tilde{v}_\theta}{\partial \eta^2} + \tilde{v}_\eta \frac{\partial^2 \tilde{v}_\eta}{\partial \eta^2} + \tilde{v}_\xi \frac{\partial^2 \tilde{v}_\xi}{\partial \eta^2}\right) d\xi}_{\mathrm{II}}$$

$$+ \underbrace{\int_0^\infty \left(\tilde{v}_\theta \frac{\partial^2 \tilde{v}_\theta}{\partial \xi^2} + \tilde{v}_\eta \frac{\partial^2 \tilde{v}_\eta}{\partial \xi^2} + \tilde{v}_\xi \frac{\partial^2 \tilde{v}_\xi}{\partial \xi^2}\right) + \frac{1}{\eta^2 \sin^2 \psi}\left(\tilde{v}_\theta \frac{\partial^2 \tilde{v}_\theta}{\partial \theta^2} + \tilde{v}_\eta \frac{\partial^2 \tilde{v}_\eta}{\partial \theta^2} + \tilde{v}_\xi \frac{\partial^2 \tilde{v}_\xi}{\partial \theta^2}\right) d\xi}_{\mathrm{II}}$$

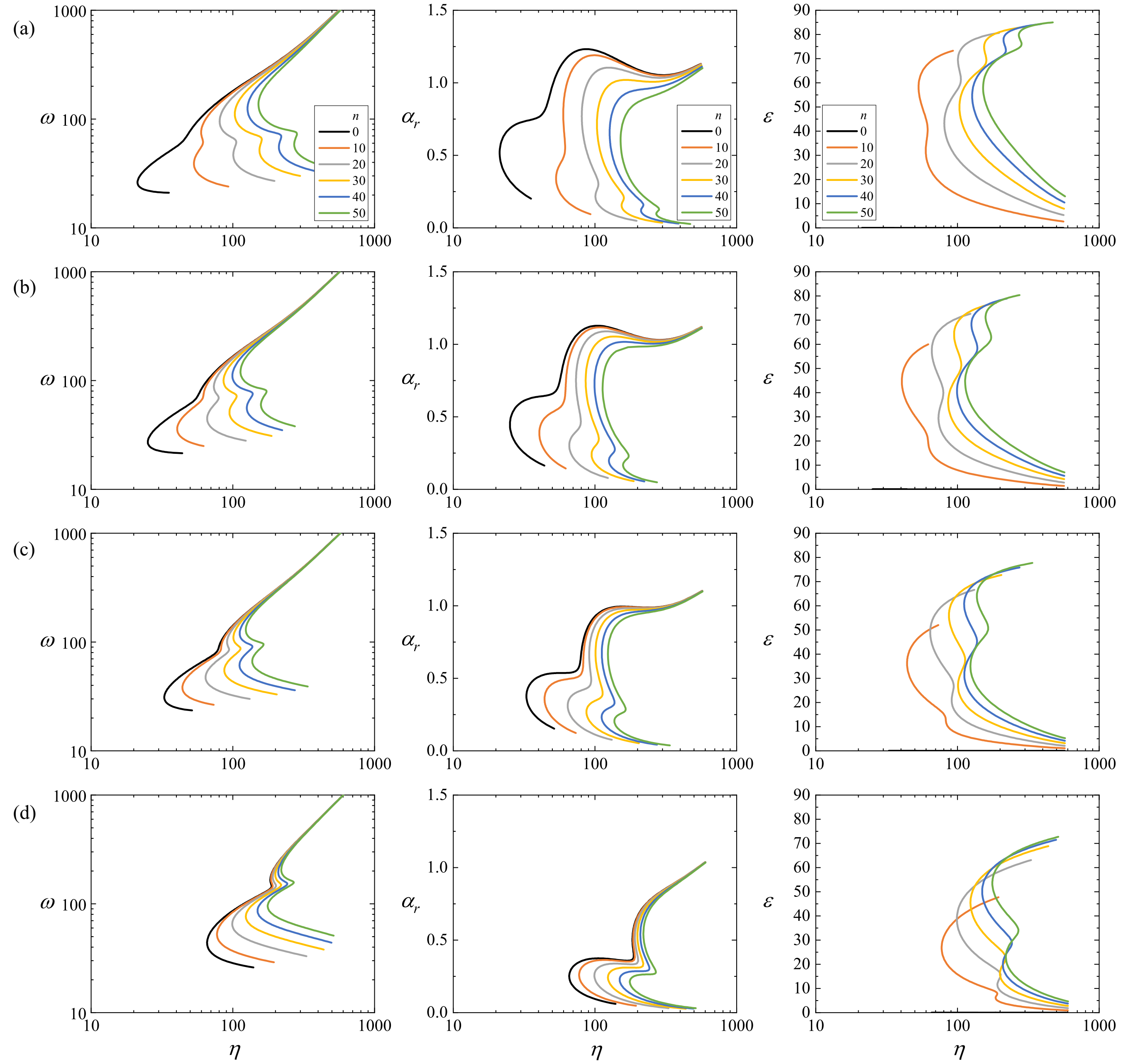

FIG. 7. Neutral stability diagrams for Gr = 30: (a) $\psi = 20^\circ$, (b) $\psi = 40^\circ$, (c) $\psi = 60^\circ$, (d) $\psi = 80^\circ$. In each case, the neutral curves are shown in the (ω, η), (α_r, η), and (ε, η) planes. (b) is equivalent to Fig. 4 and ε in the third column is in degrees.

$$-\underbrace{\int_0^\infty\left[v_{\xi 0}\frac{\partial K}{\partial \xi}+\left(\tilde{v}_\eta^2+\tilde{v}_\theta^2\right)\frac{v_{\eta 0}}{\eta}+\tilde{v}_\theta^2\frac{v_{\xi 0}}{\eta\tan\psi}\right]d\xi}_{\text{III}}+\underbrace{\int_0^\infty(\eta\mathrm{Gr}\tilde{v}_\eta\tilde{T}-\eta\tan\psi\,\mathrm{Gr}\tilde{v}_\xi\tilde{T})d\xi}_{\text{IV}}$$

$$+\underbrace{\int_0^\infty\left(\frac{1}{\eta}\frac{\partial K}{\partial \eta}+\frac{1}{\eta\tan\psi}\frac{\partial K}{\partial \xi}\right)d\xi}_{\text{VI}}-\underbrace{\int_0^\infty\left(\frac{1}{\eta\sin\psi}\tilde{v}_\theta\frac{\partial \tilde{P}}{\partial \theta}+\tilde{v}_\eta\frac{\partial \tilde{P}}{\partial \eta}+\tilde{v}_\xi\frac{\partial \tilde{P}}{\partial \xi}\right)d\xi}_{\text{V}}, \qquad (14)$$

where $K = (\tilde{v}_\eta^2 + \tilde{v}_\theta^2 + \tilde{v}_\xi^2)/2$ represents the disturbance kinetic energy. On the left-hand side, (A) represents the kinetic energy convected by the streamwise component of the basic flow. On the right-hand side, (I) represents the energy production by the shear of the basic flow. If (I) is positive, disturbance energy is gained from the basic velocity field, (II) the viscous

TABLE I. Critical values of parameters for $\mathrm{Gr} = 30$ and $\psi = 20^\circ \sim 80^\circ$ in 20° increments by fixing $n = 0$.

ψ	η_c	ω_c	α_{rc}	c	$v_{\eta 0\max}$
20°	21.25	26.0	0.51	50.84	52.70
40°	25.11	27.0	0.44	61.28	62.27
60°	32.83	31.0	0.38	82.18	81.42
80°	65.83	43.5	0.25	174.76	163.26

dissipation energy removal, (III) the streamline curvature effects, (IV) as the gain of disturbance kinetic energy through the action of buoyancy forces, (V) the pressure work. The order of (VI) is far less than others; as a result, it could be neglected.

Equation (14) is normalized by the integrated mechanical energy, then we take the real part. When the energy production exceeds the energy dissipation from the system, the disturbance will be amplified, which corresponds to a negative streamwise direction growth rate $\alpha_i < 0$:

$$\begin{aligned} -\alpha_i = {} & \underbrace{(S_1 + S_2)}_{\mathrm{I}} + \underbrace{(D_1 + D_2)}_{\mathrm{II}} + \underbrace{(G_1 + G_2 + G_3 + G_4)}_{\mathrm{III}} \\ & + \underbrace{(B_1 + B_2)}_{\mathrm{IV}} + \underbrace{(PW_1 + PW_2 + PW_3)}_{\mathrm{V}} + \underbrace{(N_1 + N_2)}_{\mathrm{VI}}. \end{aligned} \tag{15}$$

The full energy balance with the terms given in Eq. (15) for parameters marked with the circle and triangle in Fig. 4(c) is depicted in Fig. 8. For the type-I mode, it is elucidated that the major production is related to the contribution of buoyancy forces and the energy removal is dominated by viscous dissipation. So, branch 1 in Fig. 5 is mainly affected by buoyancy forces (i.e., the buoyancy-driven instability). Though subdominant, the shear production term I is still significant. Without it, the mode would be damped. For the type-II mode, the energy production (I) and reduction from viscous dissipation (II) are the dominant terms. When buoyancy effects are neglected, branch 2 in Fig. 5 apparently does not change, which is consistent with the previous analysis for eigenfunctions (the shear instability). The pressure work terms (V) are negligibly small in energy production. Meanwhile, it is worth noting that the action of the streamline curvature effect on both these two modes is to bring energy reduction, which implied that the action of streamline curvature effect stabilizes these two modes. Furthermore, the streamline curvature effect is more obvious in the type-I mode than the type-II mode (see Fig. 8). The energy dissipation caused by streamline curvature accounts for 34.95% of the total dissipation in the type-I mode, while the value was 16.30% in the type-II mode. Only the energy budget for specific parameters is shown in Fig. 8. In fact, in the same mode family, the energy budget corresponding to other critical parameters is also calculated. The results show that although the specific values of each term can be different, there is no qualitative change in the overall proportion. Consequently, we conclude that the type-I mode arises from the streamline curvature and buoyancy effects while the type-II mode arises from the inviscid effect of shear.

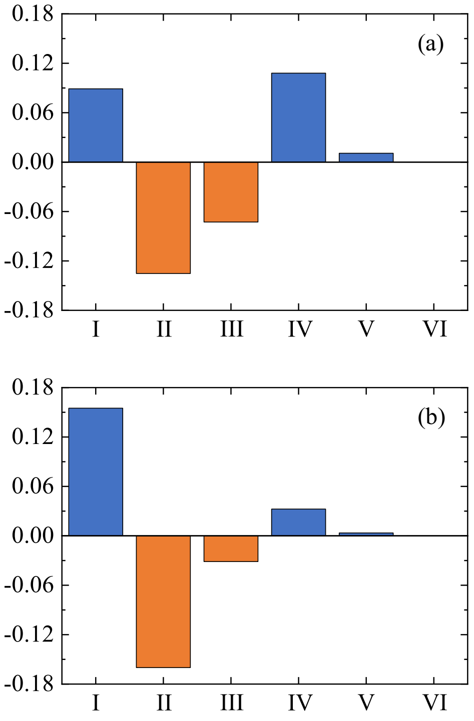

FIG. 8. Energy balance terms in Eq. (15) for (a) type-I mode and (b) type-II mode with the parameters marked with circle and triangle in Fig. 5(c).

VI. CONCLUSION

In this paper, we have studied the local linear instability of the natural convection flow around a vertically cooled cone, where the ambient fluid and the cone have independent temperature gradients. First, a physical model of the buoyancy-driven boundary layer has been proposed and a self-similar solution of the basic flow has been obtained. It is shown that when the Grashof number increases, the buoyancy boundary layer becomes thinner. Based on the linear instability analysis regime with the coupled Orr-Sommerfeld equation and energy equation, the effects of typical physical parameters, including the Grashof number Gr, streamwise location η, and half-apex angle ψ on the onset of instability have been investigated. Similar to the previous work [14], the neutral curves have higher and lower wave-number parts and present the two-lobed structure. It is also illustrated that there is no stationary mode and varying Gr only has quantitative effects on stability analysis. Additionally, the effect of varying ψ on the neutral curves has been investigated. It is shown that increasing the half angle causes the critical streamwise location η to increase and reduces the range of unstable wave number.

A typical case with $\mathrm{Gr} = 30$ and $\psi = 40^\circ$ is utilized to gain insight into mechanisms behind the buoyancy-driven flow. According to the progression of the two spatial branches in the (α_i, α_r) planes, the primary instability on the surface of the cone is identified as type-I and -II modes. By analyzing the profiles of eigenfunctions and the energy budget of these two modes, the instability mechanism of this kind of flow is obtained. Apart from the viscous dissipation, the streamline curvature and buoyancy-driven effects are dominant in the type-I mode while inviscid shear instability effects play an essential role in the type-II mode. These encouraging results are expected to be helpful in understanding the instability characteristics for such a buoyancy-driven flow system.

ACKNOWLEDGMENT

This work was supported by the NSFC (No. 12072177).

---

[1] L. Prandtl, *Essentials of Fluid Dynamics* (Blackie, London, 1952).
[2] R. B. Stull, *An Introduction to Boundary Layer Meteorology* (Kluwer Academic Publishers, Dordrecht, 1988).
[3] A. E. Gill, J. Fluid Mech. **26**, 515 (1966).
[4] A. E. Gill and A. Davey, J. Fluid Mech. **35**, 775 (1969).
[5] P. A. Iyer, Boundary-layer meteorology **5**, 53 (1973).
[6] P. A. Iyer and R. E. Kelly, ASME. J. Heat Transfer. **100**, 648 (1978).
[7] Y. Jaluria and B. Gebhart, J. Fluid Mech. **66**, 593 (1974).
[8] Y. Jaluria and K. Himasekhar, Comput. Fluids **11**, 39 (1983).
[9] A. Kulkarni, H. Jacobs, and J. Hwang, Int. J. Heat Mass Transf. **30**, 691 (1987).
[10] L. Krizhevsky, J. Cohen, and J. Tanny, Phys. Fluids **8**, 971 (1996).
[11] B. Gebhart, Y. Jaluria, R. L. Mahajan, and B. Sammakia, *Buoyancy-Induced Flows Transport* (Hemisphere, New York, 1988).
[12] G. Desrayaud, Report No. 1990/LT/01, CNAM (1990).
[13] J. Tao, P. LeQuéré, and S. Xin, Phys. Rev. E **70**, 066311 (2004).
[14] J. Tao, P. LeQuéré, and S. Xin, J. Fluid Mech. **518**, 363 (2004).
[15] X. Xiong and J. Tao, Appl. Math. Mech. **38**, 779 (2017).
[16] J. Tao and F. H. Busse, Eur. J. Mech. B Fluids **28**, 532 (2009).
[17] H. J. Merk and J. A. Prins, Appl. Sci. Res. **4**, 11 (1953).
[18] H. J. Merk and J. A. Prins, Appl. Sci. Res. **4**, 195 (1954).
[19] H. J. Merk and J. A. Prins, Appl. Sci. Res. **4**, 207 (1954).
[20] R. G. Hering and R. J. Grosh, Int. J. Heat Mass Transf. **5**, 1059 (1962).
[21] R. G. Hering, Int. J. Heat Mass Transf. **8**, 1333 (1965).
[22] T. Y. Na and J. P. Chiou, Appl. Sci. Res. **35**, 409 (1979).
[23] R. S. R. Gorla, W. R. Schoren, and H. S. Takhar, Acta Mech. **61**, 139 (1986).
[24] M. Alamgir, ASME. J. Heat Transfer. **101**, 174 (1979).
[25] T. Watanabe, Acta Mech. **87**, 1 (1991).
[26] H. S. Takhara, A. J. Chamkhab, and G. Nath, Int. J. Eng. Sci. **42**, 243 (2004).
[27] G. Palani, E. J. L. Kumar, and K. Kim, J. Appl. Mech. Tech. Phy. **57**, 473 (2016).
[28] P. Bapuji, K. Ekambavanan, and I. Pop, Heat Mass Transfer **44**, 517 (2008).
[29] T. V. Kármán, Z. Angew. Math. Mech. **1**, 233 (1921).
[30] R. J. Lingwood and P. H. Alfredsson, Appl. Mech. Rev. **67**, 030803 (2015).
[31] S. J. Garrett, Z. Hussain, and S. O. Stephen, J. Fluid Mech. **622**, 209 (2009).
[32] P. J. Schmid and D. S. Henningson, *Stability and Transition in Shear Flows* (Springer, New York, 2001).
[33] P. R. Nachtsheim, NASA Tech. Rep. No. NASA TN D-2089, NASA Lewis Research Center Cleveland, OH, United States, (1963).
[34] R. J. Lingwood, J. Fluid Mech. **299**, 17 (1995).
[35] G. Z. Gershuni, E. M. Zhukhovitskii, and A. A. Iakimov, J. Appl. Math. Mech. **34**, 669 (1970).
[36] G. Z. Gershuni, E. M. Zhukhovitskii, and A. A. Iakimov, J. Appl. Math. Mech. **37**, 544 (1973).
[37] A. J. Cooper, J. H. Harris, S. J. Garrett, M. Özkan, and P. J. Thomas, Phys. Fluids **27**, 014107 (2015).